

# Australia's lithospheric density field, and its isostatic equilibration

A.R.A. Aitken<sup>1</sup>, C. Altinay<sup>2</sup>, L. Gross<sup>2</sup>

<sup>1</sup> School of Earth and Environment, The University of Western Australia, Crawley, WA, Australia.

<sup>2</sup>School of Earth Sciences, The University of Queensland, St Lucia QLD 4072, Australia.

16 September 2015

## SUMMARY

Density is a key driver of tectonic processes, but it is a difficult property to define well in the lithosphere because the gravity method is non-unique, and because converting to density from seismic velocity models, themselves non-unique, is also highly uncertain. Here we use a new approach to define the lithospheric density field of Australia, covering from 100°E to 165°E, from 5°N to 55°S, and from the crust surface to 300km depth. A reference model was derived primarily from the recently released Australian Seismological Reference Model (*AusREM*), and refined further using additional models of sedimentary basin thickness and crustal thickness. A novel form of FEM-based deterministic gravity inversion was applied in geodetic coordinates, implemented within the open-source *escript* modelling environment. Three spatial resolutions were modelled: half-, quarter- and eighth-degree in latitude and longitude, with vertical resolutions of 5km, 2.5km and 1.25km respectively. Parameter sweeps for the key inversion regularization parameters show that parameter selection is not scale-dependent. The sweep results also show that finer resolutions are more sensitive to the uppermost crust, but less sensitive to the mid- to lower-crust and uppermost mantle than lower resolutions. All resolutions show similar sensitivity below about 100km depth. The final density model shows that Australia's lithospheric density field is strongly layered but also has large lateral density contrasts at all depths. Within the continental crust, the structure of the middle and lower crust differs significantly from the crystalline upper crust, suggesting that the tectonic processes or events preserved in the deep crust differ from those preserved in the shallower crust. The lithospheric mantle structure is not extensively modified from the reference model, but the results reinforce the systematic difference between the density of the oceanic and continental domains, and help identify subdivisions within each. The lithospheric static pressure field was resolved in 3D from the gravity and density fields. The pressure field model also highlights the fundamental difference between the oceanic and continental domains, with the former possessing lower pressure through most of the model. Overall pressure variability is large in the upper crust (60MPa) but reduces significantly by –30km elevation (20–30MPa). By –50km elevation, thick lower-crust generates further disequilibria (25–35MPa) that are not compensated until –125km elevation (10–20MPa). Beneath –125km elevation higher pressure is observed in the continental domain, extending to the base of the model. This indicates a lithosphere that is to a large degree isostatically compensated near the base of the felsic-intermediate continental crust, and again near the theoretical base of mature oceanic lithosphere.

**Key words:** Gravity, Inversion, Australia, AuSREM, Pressure, Isostasy

## 1 INTRODUCTION

Density is a fundamental property of the lithosphere and, due to large-magnitude buoyancy forces, is a very important driver of tectonic activity. The direct consequences of this density field on the Earth's gravitational acceleration field and the equipotential geoid surface are precisely-measured in high-resolution at the Earth's surface and from space (e.g. Tapley et al. 2004; Pavlis et al. 2012; Pail et al. 2011; Förste et al. 2013). Despite these high-resolution gravity-field models, density remains a difficult physical property to define within the deep lithosphere because physics does not sup-

port a unique solution to the gravity inverse-problem, except under highly idealised scenarios. Therefore, gravity-only models of the crustal or lithospheric density field, Moho geometry etc. require assumptions that inherently produce uncertain and often biased results (see the review by Aitken et al. 2013). Seismic tomographies provide a robust and complementary capability to resolve 3D lithospheric structure, although they possess their own uncertainties and biases (see review by Foulger et al. 2013). Furthermore, converting seismic velocities to density is highly uncertain, involving further assumptions (e.g. Brocher 2005).

Nonetheless, several methods have been developed to model

the Earth's density structure in the deep lithosphere and mantle, combining gravity data with seismic tomographies and other datasets, such as topography, surface heat flux, and mineral physics models constrained by data from xenolith databases (e.g. Kaban et al. 2014; Tesauro et al. 2014; Afonso et al. 2013a,b; Fullea et al. 2009; Simmons et al. 2010). Due to a combination of technical limitations and research interest, such approaches have typically focused on modelling the density of the mantle, with the gravity effects of the crust either treated as a single layer or removed prior to inversion (e.g. Kaban et al. 2014; Simmons et al. 2010). One reason for this separate approach is that the density in the mantle can feasibly be related to variations in temperature and compositional variations (e.g. Kaban et al. 2014; Afonso et al. 2013a,b; Fullea et al. 2009; Simmons et al. 2010). These properties are much harder to define for the crust (Afonso et al. 2013b), which possesses much more compositional heterogeneity and also more complex thermal structure due to crustal heat production. Furthermore, with typical array geometries, teleseismic tomographies are most sensitive to mantle structure (Foulger et al. 2013). At continent-scale, the structure of the crust is commonly derived from compilations of more locally derived information (e.g. Salmon et al. 2013b), although ambient noise tomography provides significant capability to generate crust-focused tomographies from larger seismic arrays (e.g. Salmon et al. 2013a).

To help resolve this disconnect between crust and mantle modelling, we seek a method appropriate for whole-of-lithosphere modelling, including both the deep lithosphere and detailed crustal structure in one single high-resolution model, also including 3D information from several seismic datasets. A robust and flexible computational approach to achieve this has not been openly available. Here we describe a new approach to 3D gravity inversion in a geodetic coordinate system that takes into account the ellipsoidal shape of the Earth (see Appendix A). This approach is implemented in the open-source *escript* modelling environment (Gross et al. 2007). *escript* is fully parallelised with OpenMP and MPI and massively scalable, allowing very large computational problems to be undertaken (see Gross & Kemp 2013; Gross et al. 2015).

Including the *AuSREM* seismological model (Kennett & Salmon 2012) as well as models of crustal thickness (Aitken et al. 2013; Laske et al. 2012) and sedimentary basin thickness (Frogtech 2005; Laske et al. 2012) as initial inputs, we apply this method to the Australian region to generate whole-of-lithosphere scale model of the density field. Finally, we compute the static lithospheric pressure field of the region. The results highlight some of the characteristics that define the past evolution and current state of the Australian continent.

## 2 MODEL SETUP

The model region spans from  $100^{\circ}\text{E}$  to  $165^{\circ}\text{E}$  and from  $5^{\circ}\text{N}$  to  $55^{\circ}\text{S}$ . Allowing room for “edge effects”, this region encompasses the entirety of the Australian continent, as well as its surrounding oceans and orogenic belts (Figure 1). In accordance with *AuSREM* we extend the active model to a depth of approximately 300km below the topographic surface.

We use three model resolutions. Our moderate resolution model has a lateral resolution of  $0.5^{\circ}$  with 5km depth resolution, comparable to the resolution of the *AuSREM* model, and with a total of about 0.94 million active cells. We also generate a high resolution model at  $0.25^{\circ}$  with 2.5km depth resolution (about 7.5 million cells) and a very high resolution model at  $0.125^{\circ}$  with 1.25km

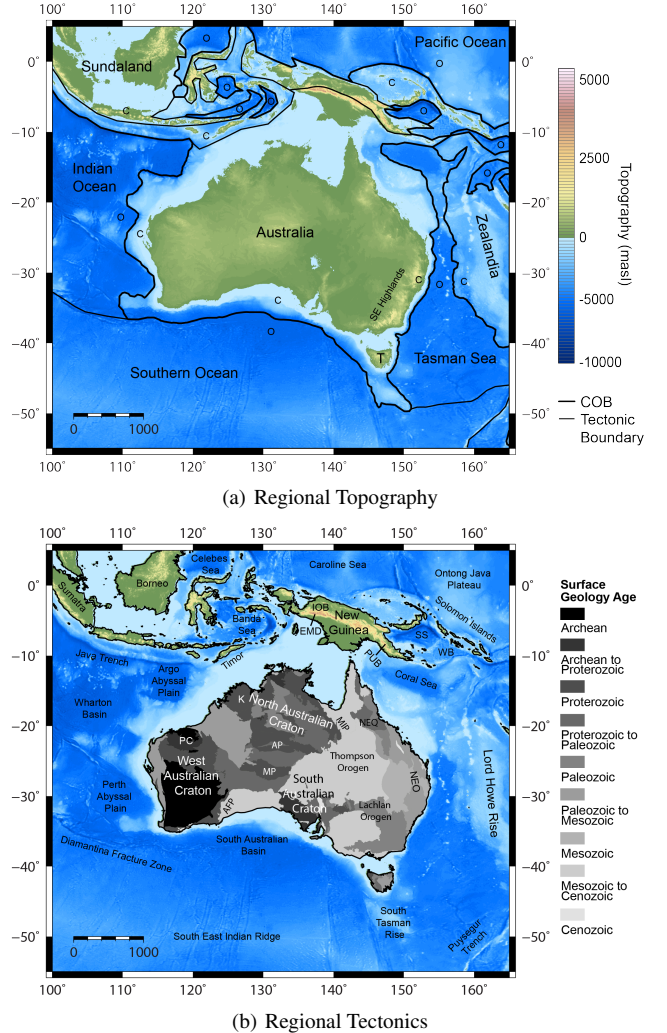


**Figure 1.** (a) Topography in the region, including plate-scale tectonic regions and continent-ocean boundary (COB) interpretations - o indicates oceanic, c indicates continental; data from ETOPO1 (Amante & Eakins 2009) T - Tasmania (b) The tectonics of the region with major regions and features labelled. AFP - Albany Fraser Province; AP - Arunta Province; EMD - Ertsberg mining district; IOB - Irian Ophiolite Belt; K - Kimberley Craton; MIP - Mt Isa Province; MP - Musgrave Province; NEO - New England Orogen; NEQ - North East Queensland; PUB - Papuan Ultramafic Belt; SS - Solomon Sea; WB - Woodlark Basin.

depth resolution (about 60 million cells) to take advantage of the capability of the high-resolution gravity data to resolve crustal density structure.

### 2.1 Gravity Data

To drive the inversion we use the combined satellite/near-surface gravity model *Eigen6C3stat* (Förste et al. 2013). The *Eigen6C3stat* model includes satellite gravity data from *LAGEOS* and *GRACE*, satellite gradiometry data from *GOCE* and near-surface gravity data from the *DTU10/12* models (Förste et al. 2013). The *DTU10/12* models are derived from satellite altimetry offshore, and from the *EGM2008* model onshore (Pavlis et al. 2012). *EGM2008* is high quality for Australia, but has much lower certainty in New Guinea and Sundaland (Pavlis et al. 2012).

The gravity disturbance at the Earth's surface was computed

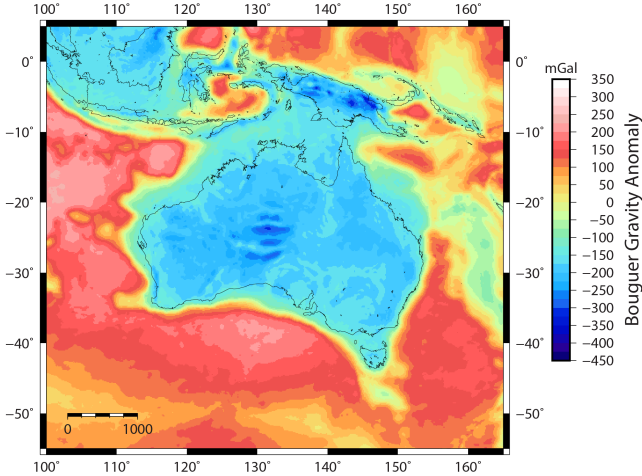


**Figure 2.** *EIGEN6C3stat* Bouguer gravity anomaly at  $\frac{1}{8}^\circ$  resolution, data upward continued by 10km.

at the relevant cell size from the spherical harmonic model to degree and order 1949 (Förste et al. 2013), approximately  $\frac{1}{11}^\circ$  resolution. From this fully resolved model, the lowest order components were removed by subtracting a separately computed regional gravity disturbance model containing only the lower-orders of the same model. The regional gravity disturbance was computed in full to degree and order 10, and with a gentle-cut filter from degree and order 10 to 15 to avoid Gibb's oscillations (Förste et al. 2013). The regional field is characterised by a northwest-southeast trend with a low to Australia's southwest ( $-40\text{mGal}$ ) and a high extending along the convergent margin to the north ( $60\text{mGal}$ ). Thus the regional gravity disturbance represents mostly upper-mantle density variations related to high density subducted slabs, whereas the residual gravity disturbance represents mostly lithospheric density variations.

The wavelength-range chosen for the regional is  $12^\circ - 18^\circ$ , approximately 1300 – 2000 km, and does not provide a perfect separation of the lithosphere-derived gravity field from the upper-mantle-derived gravity field. Shorter-wavelength density heterogeneity in the upper mantle, for example from localised upwellings, and longer wavelength components of the lithospheric density field, e.g. major sedimentary basins, cratons, overlap in wavelength. Lithosphere-derived gravity anomalies are not plainly visible in the regional data, but may exist as a minor component. Similarly, upper-mantle derived gravity anomalies are not plainly visible in the residual dataset, but may exist and may be important. For example significant gravity anomalies may remain from mantle upwellings in eastern and southern Australia (Czarnota et al. 2014).

To reduce the free-air anomaly at the Earth's surface to the much less topography dependent Bouguer anomaly, we apply three standard corrections. Firstly we apply an infinite slab-correction, secondly a curvature correction (after Lafehr 1991) that modifies the previous correction so as to define a spherical-cap of radius 166.7 km. We apply a 3D terrain correction from theETOPO1 digital terrain model grid. The terrain response is calculated at the relevant data elevation for each data-grid cell using a flat-Earth approximation method suitable for airborne data (Nowell 1999). We include topographic variations out to 300 km distance. All topography exists beneath the model data-elevation, and so errors from the flat-Earth approximation are restricted to the very small errors in distance and angle due to the curvature of the Earth. These errors

do not exceed 0.3% of the overall terrain correction value (Nowell 1999).

All the above corrections assume a density of  $2670 \frac{\text{kg}}{\text{m}^3}$  for rock and  $1030 \frac{\text{kg}}{\text{m}^3}$  for water. The assumption of a single density value everywhere causes some artifacts where density does not accord to this value, for example at seamounts and mid-ocean ridges (Figure 2). To avoid excessive sensitivity to the mesh geometry, and to reduce topography artefacts, the Bouguer gravity data were upward-continued to a level commensurate with the model resolution; 25km, 15km and 10km for the moderate, high and very high resolution models respectively. Upward continuation was implemented through a fourier transform approach in the GMT package (Wessel et al. 2013).

The residual Bouguer gravity data (Figure 2), show the main lithospheric divisions of the region. Most notable is the distinction between oceanic and continental lithosphere. Also evident are the internal divisions within continental Australia, including major sedimentary basins and crustal uplifts of central Australia, and the complex structure of the convergent margin to the North. Within the oceanic regions, the gravity data resolve clearly a relationship with oceanic lithosphere age (Müller et al. 2008).

## 2.2 The AuSREM reference model

To constrain the gravity inversion result, and especially the vertical stratification of the lithosphere, we rely upon several previously published models. Fundamentally we assume three layers: sedimentary basins, crystalline crust and mantle.

The first boundary (Fig. 3(a)) is defined for the majority of the Australian continent by the *SEEBASE* model, from which we obtain the thickness of Phanerozoic sedimentary basins (Frogtech 2005). Proterozoic basins are not included due to their highly variable density, often reflecting metamorphic grade from orogenic events. Outside of the *SEEBASE* model extents (see Fig. 3(a)) we use the sedimentary thickness of the *CRUST 1.0* model (Laske et al. 2012). Although the two models are broadly compatible, sedimentary rock thickness differences are significant at some points on the boundary.

Density within the sedimentary layer is defined by an exponential compaction law (Table 1) assuming quartz grain-density and saline water fluid-density. In the moderate resolution model the 5km vertical resolution of the model severely limits our ability to incorporate important variations in sedimentary basin thickness, but this is much less pronounced for the high and very high resolution models.

The thickness of the crust (Fig. 3(b)) for most of the region is derived from the mean Moho elevation from the gravity-seismic-isostatic model of Aitken et al. (2013) and the topographic surface of ETOPO1 (Amante & Eakins 2009). This gravity inversion derived Moho model is built upon a seismic- isostatic initial model involving the *AusMoho* database of Moho picks (Salmon et al. 2013b), with an isostatic initial Moho model elsewhere. This model has a lateral resolution of 20km, and a vertical  $2\sigma$ -error (inversion variability) of between 1km and 7km (Aitken et al. 2013). Outside of this region we use the *CRUST 1.0* model of crustal thickness (Laske et al. 2012). For the region in which it is relied upon, *CRUST 1.0* is derived mostly through extrapolation, but the two models are largely compatible for the Indian Ocean, Sundaland and Pacific segments. The Southern Ocean however has significant discrepancies, including at the South Tasman Rise, and in the southwest (Figure 3(b)).

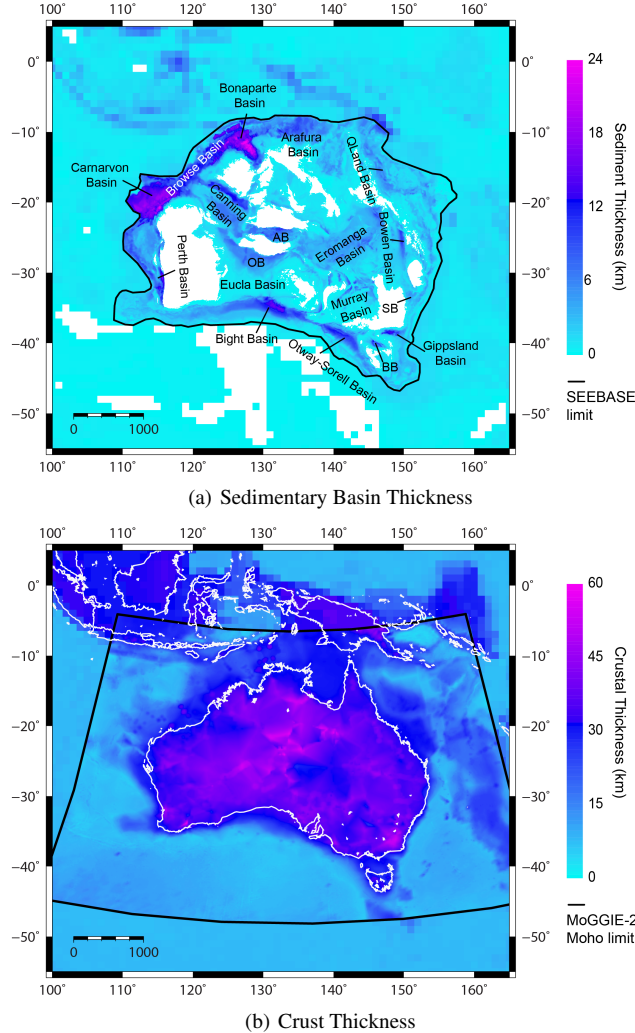


**Figure 3.** (a) The thickness of sedimentary rocks in the region from the SEEBASE and CRUST1 models. AB - Amadeus Basin; BB - Bass Basin; OB - Officer Basin; SB - Sydney Basin. Both models show broadly comparable thicknesses (b) the thickness of the crust from the MoGGIE-2 model of Aitken et al. (2013) and CRUST1. Agreement between the two models is reasonable except for the Southern Ocean

Layer	Rule Based
Sedimentary Basins	$2650 \cdot (1 - \phi) + 1030 \cdot \phi$ with $\phi = 0.4 \cdot e^{0.3 \cdot (h - 2.5)}$
Crystalline Continental Crust <sup>1</sup>	$2670 - 8 \cdot h$
Oceanic Crust	2890
Mantle ( $h > -50\text{km}$ )	$3300 - 0.2 \cdot (h + 150)$
Mantle <sup>2</sup> ( $-50\text{km} \geq h > 150\text{km}$ )	$3300 - 0.2 \cdot (h + 150)$
Mantle <sup>2</sup> ( $h \leq -150\text{km}$ )	$3300 - 1.54 \cdot (h + 150)$

<sup>1</sup> density defined by AusCrust within its extents, rule based elsewhere;

<sup>2</sup> density defined by AusMantle within its extents, rule based elsewhere

**Table 1.** Density models in  $\frac{\text{kg}}{\text{m}^3}$  and rules used for the reference model,  $h$  is negative downwards in km,  $\phi$  is porosity. The coefficients for the rule-based crystalline crust and mantle density models are based on best-fit linear regressions through the crust and mantle components of the AuSREM model (Kennett et al. 2013; Salmon et al. 2013a)

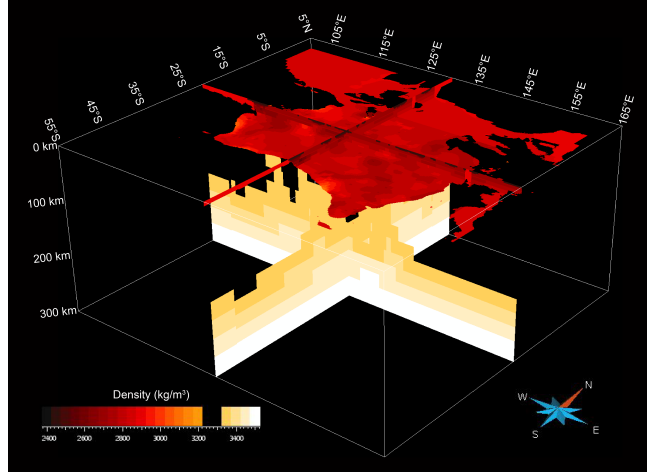


**Figure 4.** Reference model at very high resolution. Vertical exaggeration is  $\approx 10$ . Densities within the range  $3275 \pm 50 \frac{\text{kg}}{\text{m}^3}$  have been made transparent for visualisation

For longitudes between  $110^\circ\text{E}$  and  $160^\circ\text{E}$ , and for latitudes between  $10^\circ\text{S}$  and  $45^\circ\text{S}$  density within the crystalline crust is derived from the *AusCrust* model (Salmon et al. 2013a). The *AusCrust* model above  $10\text{km}$  depth includes the oceans, which we do not model, and so these shallow layers were excluded from the reference model. Outside of this region continental crust is uniformly assigned an increasing density with depth using the best-fit linear regression through *AusCrust* (Table 1). Oceanic crust is delineated as in Figure 1 using the continent-ocean boundary interpretation of Seton et al. (2012), and is assigned a density of  $2890 \frac{\text{kg}}{\text{m}^3}$  (Carlson & Raskin 1984).

For longitudes east of  $105^\circ\text{E}$  and for latitudes between  $0^\circ\text{S}$  and  $50^\circ\text{S}$ , and depths below  $50\text{km}$ , we define the mantle density using the *AusMantle* density model (Kennett et al. 2013). Outside of, and above, the *AusMantle* region, we define mantle density through a simple velocity function involving two linear trends, each based on best-fit linear regressions through the *AusMantle* model. In the *AusMantle* model, the overall velocity increases slowly with depth until  $150\text{km}$  depth, after which a more rapid increase is observed to the base of the model, see Table 1 for the laws used.

The density model is realised in a 3D voxel binary format suitable for input into *escript*, see Figure 4. The final *escript* domain also includes an air layer extending to  $55\text{km}$  above the surface, within which the data grids exist. In this region we evaluate the gravity field, but the density model is locked at zero. The data grids are located, so far as mesh-dimensions permit, at the elevation above the surface corresponding to the upward continuation distance plus bathymetry. In addition, we add a  $300\text{km}$  thick zone beneath the base of the model to minimise the influence of the basal boundary conditions on the model results. Like the air layer, we compute the 3D gravity field in this zone, but the density model is locked at  $3531 \frac{\text{kg}}{\text{m}^3}$ , which is the value at  $300\text{km}$  depth using the linear regression model (Table 1).

At moderate resolution, the overall RMS gravity misfit of this reference model is  $344.3\text{mGal}$ , considerably greater than the RMS variability of the observed data values ( $135.0\text{mGal}$ ). At high and very high resolution the initial model RMS misfit is  $348.2\text{mGal}$  and  $343.0\text{mGal}$  respectively, so this misfit cannot easily be ascribed to the model resolution. Significant modifications to the reference model are required to explain the observed gravity field, and these are achieved through a new geophysical inversion method.

### 3 INVERSION METHODOLOGY

In our inversion methodology we follow established routines for a deterministic gravity inversion approach (e.g. Li & Oldenburg 1998). We minimize a cost function incorporating several terms to obtain a density correction to a reference model. The terms of this cost-function describe the misfit to the gravity data, the magnitude of the density correction, and the degree of smoothness of the density correction. The problem is formulated and solved using an orthogonal geodetic coordinate system (Featherstone & Claessens 2008) in geodetic latitude  $\phi$ , longitude  $\lambda$  and height  $h$  relative to the geodetic zero, see Appendix A. The solution method is implemented using the 3D finite element method with optimization for massively parallel computing (Gross & Kemp 2013; Gross et al. 2015).

The cost function is reduced through an iterative process which is terminated when the relative change to the density correction reaches a given tolerance; we use  $10^{-3}$ .

The density distribution is to be recovered from the relative gravity data  $f_h$  along the geodetic height coordinate line measured near the geodetic zero level  $h = 0$ . The density is parameterized using a property function  $m$  as a density proxy in the form

$$\hat{\rho} = \rho_{ref} + \rho' \cdot m \quad (1)$$

where  $\rho' = 2750 \frac{kg}{m^3}$  is a scaling factor and  $\rho_{ref}$  is the reference density model minus its mean  $\bar{\rho}$  which depends a little on model resolution but is  $\approx 3420 \frac{kg}{m^3}$ , see Section 2.2.

In applying this property function we do not choose to apply an artificial depth weighting, although the capability exists within *script*. Such depth weighting is commonly used to counteract the reduction in gravity sensitivity with depth (e.g. Li & Oldenburg 1998). In our work, model depth sensitivities are defined by the gravity method and the modifications on this imposed by the model domain and resolution length-scales and the trade-off parameters  $\mu_1$  and  $\mu_0$ , see Sections 4 and 6.2.

The inversion process minimizes the cost function given in the form

$$J(m) = J^{(d)}(g_h) + \mu_1 \cdot J^{(1)}(m) + \mu_0 \cdot J^{(0)}(m) \quad (2)$$

over all admissible property functions  $m$ . The argument  $g_h$  is the predicted vertical gravity due to the density  $\hat{\rho}$  as in equation (1). The factors  $\mu_1$  and  $\mu_0$  are trade-off factors discussed in detail later. The term  $J^{(1)}$  denotes the  $H^1$ -regularization term measuring the smoothness of the correction to the reference model. It is used in the form

$$\begin{aligned} J^{(1)}(m) = & \frac{1}{2} \int_{\Omega} \left( w_{\lambda} \cdot \left( d_{\lambda} \frac{\partial m}{\partial \lambda} \right)^2 \right. \\ & \left. + w_{\phi} \cdot \left( d_{\phi} \frac{\partial m}{\partial \phi} \right)^2 + w_h \cdot \left( d_h \frac{\partial m}{\partial h} \right)^2 \right) V d\phi d\lambda dh \end{aligned} \quad (3)$$

where  $w_{\lambda}$ ,  $w_{\phi}$ , and  $w_h$  are directional, potentially spatially variable, weighting factors. The factors  $V$  and  $d_{\alpha}$  for  $\alpha = \phi, \lambda, h$  include the geodetic coordinate system, see Appendix A. Note that model smoothness in  $\phi$ ,  $\lambda$  and  $h$  can be manipulated within this term for anisotropic regularization (see Section 4.2).

The  $L^2$ -regularization term  $J^{(0)}$  is given as

$$J^{(0)}(m) = \frac{1}{2} \int_{\Omega} m^2 V d\phi d\lambda dh. \quad (4)$$

It measures the deviation of the density correction from the reference model. The data misfit component  $J^{(d)}$  of the vertical gravity

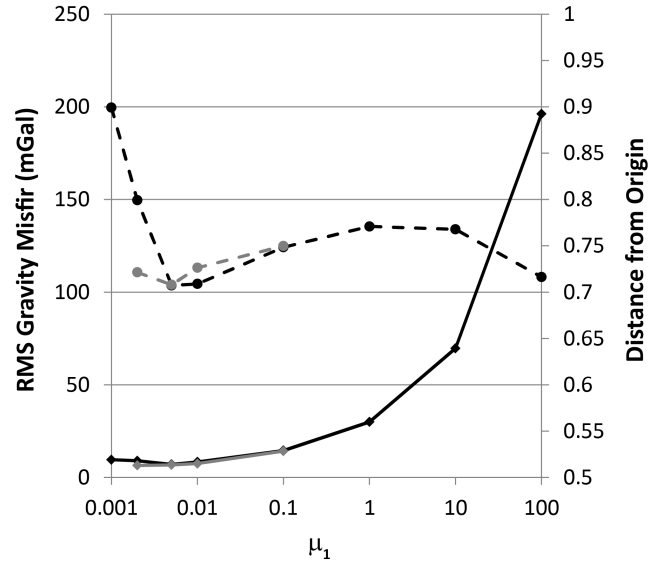


Figure 5.  $\mu_1$  sweep for moderate (black) and high (grey) resolutions, showing RMS gravity misfit (solid) and distance from origin (dashed). The optimum  $\mu_1$  for both resolutions is 0.005.

$g_h$  in the total cost function  $J$  is set as

$$J^{(d)}(g_h) = \frac{1}{2} \int_{\Omega} \chi \cdot (g_h - f_h)^2 V d\phi d\lambda dh \quad (5)$$

where  $f_h$  denotes the measured gravity normal to the geodesic zero level  $h = 0$ , see Section 2.1. The data are normalized to have zero mean. The factor  $\chi$  is the characteristic function of the locations of measurements, here assuming all measurements are obtained with the same level of confidence. The vertical gravity  $g_h$  is defined via a partial differential equation (PDE) constraint in the form

$$g_h = -d_h \frac{\partial u}{\partial h} \text{ with } -\Delta u = 4\pi G \hat{\rho} \quad (6)$$

where  $u$  is the scalar gravity potential,  $d_h$  is the scaling factor due to the use of the geodetic coordinate system (see Appendix A),  $\Delta$  refers to the Laplace operator and  $G$  denotes the gravity constant. The potential is set to zero at the top of the air layer while on all other surfaces of the domain the gravity component in direction of the surface normal is set to zero.

### 4 METHOD PROCEDURE AND MODEL VARIABILITY

The cost function in equation (2) to be minimized contains several user-specified parameters that, along with the data, determine the results. In the absence of any a-priori knowledge as to what the optimal settings are, any single set of values carries significant bias. However, if these parameters are varied sufficiently this also provides the benefit of understanding the range of models that satisfy our misfit criteria, and can therefore be considered acceptable. We build towards our final model in a series of parameter sweeps in which we attempt to find the optimum balance between data misfit, model smoothness and least change to the reference model.

#### 4.1 Trade-off parameter $\mu_1$

The most fundamental is the choice of the trade-off parameter,  $\mu_1$ , that defines the degree of importance of the  $H^1$ -regularization term of the cost function (see equations (2) and (3)).

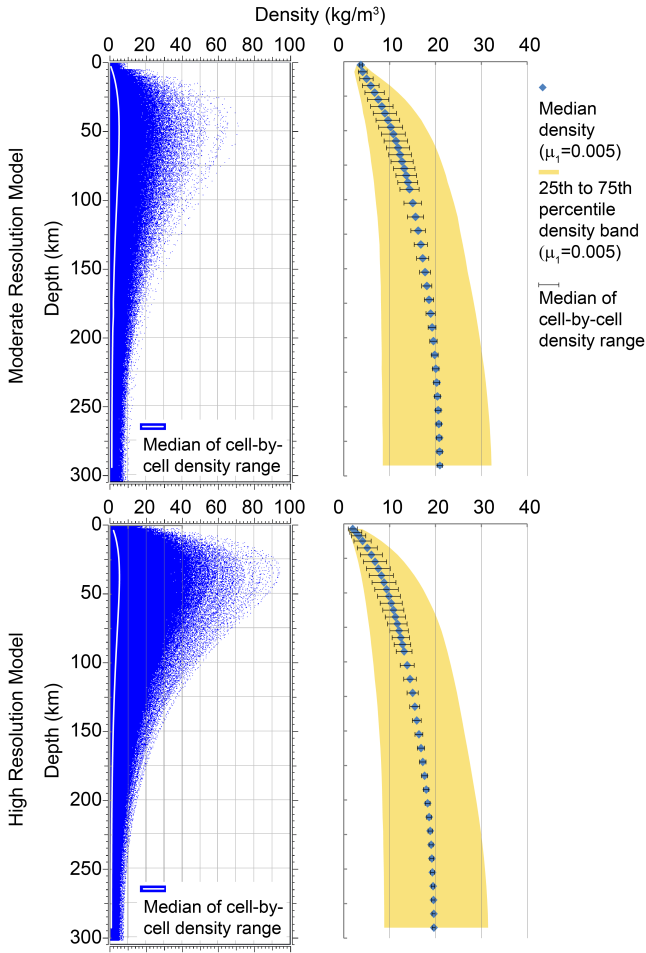


**Figure 6.** Left: Model variability (cell-by-cell range of  $m$ ) with  $\mu_1$  for the four accepted models at moderate and high resolution. For visualisation only, elevations have been uniformly randomised within one-cell height to provide an impression of occurrence frequency. The white line indicates the median range. See Figure ?? for depth-slice images of the range of  $m$ . Right: The median and 25th to 75th percentile density band of  $|m|$  analysed across all  $\lambda$  and  $\phi$  for discrete  $h$  bands. The model with  $\mu_1$  of 0.005 was used. Error bars indicate the median range across all accepted  $\mu_1$  values as shown in the left panel.

We have first conducted a parameter sweep of the  $\mu_1$  trade-off factor from 0.001 to 100 for the moderate resolution model, and a subset of those for the high resolution model (Figure 5). The trade-off factor  $\mu_0$  for the  $L^2$ -regularization is set to zero for this test. Inversion will rapidly proceed until the point is reached that the  $H^1$ -regularization term and the data-fit term are in competition. This means that very smooth density changes will be accepted by all models, but that the best data misfit typically involves a non-smooth result, and that the most stable model is often a poor fit to the data. Note that both the  $H^1$ - and  $L^2$ -regularization terms apply only to  $m$ , that is, the density correction derived from inversion and not the final density distribution.

In terms of selecting, firstly, a range of acceptable models, and secondly, the optimal model, we applied the following criteria: The upper bound, in terms of gravity data misfit, is defined by the highest value for trade-off parameter  $\mu_1$  that provides an RMS misfit of less than some chosen value. In this case we select 10% of the total gravity data variation, which for our datasets is 13.5mGal.

This value is a little more than the fit achieved in previous studies of Australia at this scale (Aitken et al. 2013; Aitken 2010). The lower bound is defined by the point at which further reduction in  $\mu_1$  does not result in significantly improved misfit, either through only minimal improvements, or caused by the onset of instability due to under-regularization.

Finally, to proceed to further testing, we must select a single optimum value for the  $\mu_1$  trade-off parameter. Aiming for a well-balanced solution, we select the value, within the above defined bounds, that provides the solution closest to the origin in  $\frac{J^{(d)}}{J}$  versus  $\frac{J^{(R)}}{J}$  space, where  $J^{(R)}$  includes the  $J^{(1)}$  and  $J^{(0)}$  terms and their trade-off parameters. In essence, this selection provides the closest match to equal weighting between the data-fit and regularization components of the cost function that is permitted by the preceding data-misfit criterion.

For the moderate resolution model we see that the range of acceptable models spans from  $\mu_1 = 0.002$  to  $\mu_1 = 0.1$  (Figure 5). Within this range, the model closest to the origin, and also possessing the lowest misfit (7.05mGal) is  $\mu_1 = 0.005$ . For the high resolution model we see virtually identical results, except at  $\mu_1 = 0.002$ , where the higher resolution permits lower misfit than was possible for the moderate resolution model. With  $\mu_1 = 0.005$  the RMS gravity misfit for the high resolution model is 6.73mGal (Figure 5).

Within this  $\mu_1$  range, the variability in the model results is relatively small (Figure 6). For both resolutions, the variability of the models obeys a smooth depth-dependent function characterised by increasing variability at upper-to-mid crustal depths, a peak at mid-crustal to upper-mantle depths and decreasing variability within the deeper mantle.

## 4.2 Anisotropic $H^1$ -regularization

Within the  $H^1$ -regularization term, there is the capability to introduce anisotropic regularization through the coefficients  $w_\lambda$ ,  $w_\phi$  and  $w_h$ . Note that, so long as the sum of these weighting components does not change, this anisotropic regularization does not affect the overall influence of  $H^1$  regularization.

Maintaining the conditions  $w_\lambda = w_\phi$ , and  $w_h + w_\lambda + w_\phi = 3$  we apply a series of 6 increments, in each of which horizontal-bias anisotropy ( $\frac{w_\lambda}{w_h}$  and  $\frac{w_\phi}{w_h}$ ) doubles from 0.5 to 32. For the moderate resolution model, these seven models show increasing RMS misfit with increasing horizontal-bias anisotropy, reaching our upper bound with anisotropy of 16 times (RMS = 13.3mGal). Reducing horizontal-bias anisotropy to 0.5 times allows slightly better data fit (by 0.6mGal). There is only a small difference in terms of the distance to origin criterion, with a slight reduction with increasing horizontal-bias anisotropy.

Variability in the model results is small. Increasing anisotropy smoothes lateral density changes, and the highest degrees of anisotropy showing visible evidence of lateral smoothing. However, increasing anisotropy does not lead to non-smooth changes in  $m$  with  $h$ , which are inherently smooth, and there is no evidence for significant changes in the depth sensitivity of the models. While anisotropic weightings in the  $H^1$ -regularization term may have utility in certain cases, in this case there is no evidence for a quantifiable improvement to the model fit. Thus we retain isotropic  $H^1$ -regularization for the remainder of the work.

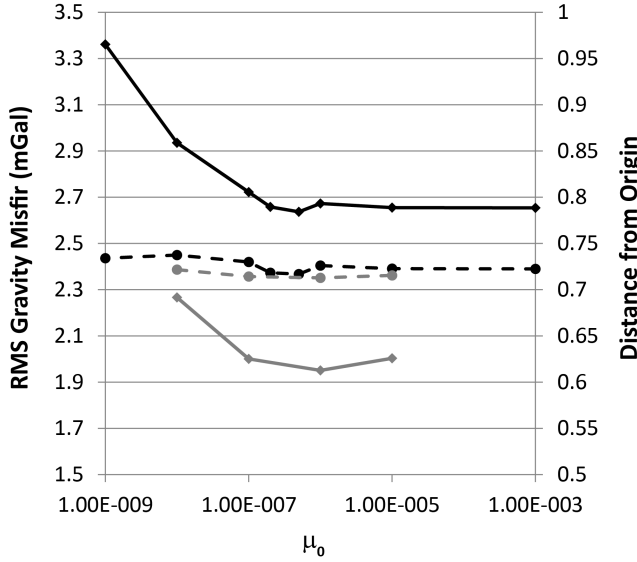


**Figure 7.**  $\mu_0$  sweep for moderate (black) and high (grey) resolutions, showing RMS gravity misfit (solid) and distance from origin (dashed). The optimum  $\mu_0$  for both resolutions is  $10^{-7}$  above which misfit gains are minimal, and erratic.

#### 4.3 Trade-off parameter $\mu_0$

Through  $\mu_0$ , we can specify the relative influence of  $L^2$ -regularization, which minimises the squared magnitude of the deviation from the reference model.

Parameter sweeps for  $\mu_0$  were performed from  $10^{-9}$  to  $10^{-3}$  for the moderate resolution model.  $\mu_1$  was maintained at 0.005. As with  $\mu_1$ , we accept all models with misfit beneath  $13.5\text{mGal}$  and with no signs of instability. In this case, increasing  $\mu_0$  allows non-smooth changes to be developed at relatively low cost. Non-smooth density changes in the upper crust are an important gravity source, so increasing  $\mu_0$  has the effect of allowing a lower data misfit and reduces the overall constraint on the model. The curve tends towards minimum values at infinity, and so we consider the optimum value to be at the point where further increase in  $\mu_0$  does not result in significantly improved misfit (at least 5% less than the previous value).

For the moderate resolution model, all models in the tested range produced a gravity data misfit that is substantially less than the threshold value, and so all are considered acceptable. The gravity data misfit reduces from  $3.36\text{mGal}$  for  $\mu_0 = 10^{-9}$  to  $2.65\text{mGal}$  for  $\mu_0 = 10^{-3}$ , although meaningful reductions are not made for  $\mu_0 > 10^{-7}$  (Figure 7). Thus, the optimum  $\mu_0$  point is reached at  $\mu_0 = 10^{-7}$ , as further de-regularization does not substantially improve data fit. Similar results were achieved at high resolution, but a lower misfit is achieved ( $2.00\text{mGal}$  for  $\mu_0 = 10^{-7}$ ). For the very-high resolution model ( $\mu_1 = 0.005, \mu_0 = 10^{-7}$ ), the misfit was reduced further to  $1.65\text{mGal}$ . Across the tested range, we see that the distance from origin criterion is fairly insensitive to  $\mu_0$ , although it generally reduces with increasing  $\mu_0$  (Figure 7).

Within the tested  $\mu_0$  range, the variability in the model results is typically small, but is occasionally quite large (Figure 8). Model variability is characterised by high variability at upper-to-mid crustal depths, and reducing variability into the mantle, with very low variability with  $\mu_0$  in the lower lithosphere.

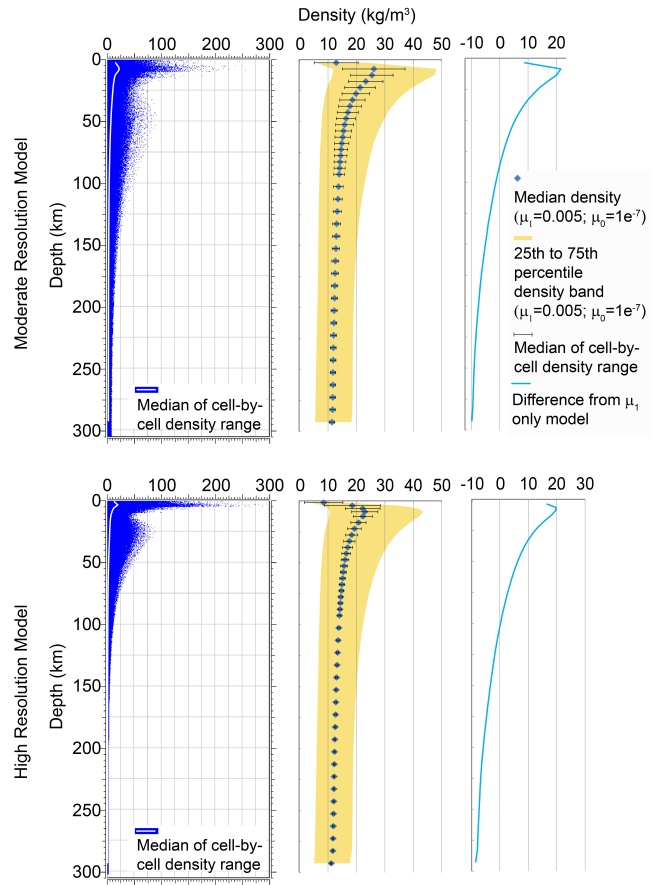


**Figure 8.** Left: Model variability (cell by cell range of  $m$ ) with  $\mu_0$  for six accepted models at moderate and four at high resolution. For visualisation only, elevations have been uniformly randomised within one-cell height to provide an impression of occurrence frequency. The white line indicates the median range. See Figure ?? for depth-slice images of the range of  $m$ . Centre: The median and 25th to 75th percentile density band of  $|m|$  analysed across all  $\lambda$  and  $\phi$  for discrete  $h$  bands. The model with  $\mu_1$  of 0.005 and  $\mu_0$  of  $10^{-7}$  was used. Error bars indicate the median range across all accepted  $\mu_0$  values as shown in the left pane. Right: Difference in median  $|m|$  with  $h$  from the model with  $\mu_1$  alone (Figure 6)

#### 5 PRESSURE ANALYSIS METHOD

Our method simultaneously and self-consistently resolves the 3D density and gravity fields, and it is a natural extension to use these to define static pressure within the region.

We recover pressure  $p$  as a function of its location in the domain from the equation

$$\Delta p = \nabla^t \mathbf{F} \quad (7)$$

where  $\mathbf{F}$  are the acting body forces due to local density and gravity. This equation is derived from the momentum balance equation under the assumption of a constant shear modulus, see Appendix B. It is pointed out that equation (7) resolves the full 3D pressure field from the included buoyancy forces and does not assume zero shear stresses. When we solve the equation for pressure  $p$  we do not include any forces from buoyancy outside the model, nor any forces applied at the base or the sides of the model. Thus this model does not include upper-mantle buoyancy forces nor those related to plate-tectonic movements.

Using the geodetic coordinate system, see Appendix A, the

body force  $\mathbf{F}$  is given as the product of density and gravitational acceleration in the form

$$F_\alpha = (\bar{\rho} + \hat{\rho}) \cdot (g_\alpha + g_\alpha^{(topo)} - g_{back} \delta_{h\alpha}) \quad (8)$$

for  $\alpha = \phi, \lambda, h$  where  $\bar{\rho}$  is the mean of the reference density model (see Section 2.2),  $\hat{\rho}$  is the density correction from the inversion (see equation (1)) and  $g_\alpha$  is the corresponding gravity acceleration vector. The component  $g_\alpha^{(topo)}$  re-introduces the gravitational attraction of topography, which is missing from the 3D model. It is obtained by solving the forward problem (6) with a topographic-mass equivalent density layer just above the surface, using densities as in the Bouguer correction.  $g_{back}$  is the depth dependent “background” vertical gravity acceleration. The Kronecker  $\delta$ -symbol,  $\delta_{h\alpha}$ , assigns zeros to the  $\phi$  and  $\lambda$  components of this vector. Assuming a spherical Earth, and thus avoiding latitudinal effects in the data,  $g_{back}$  is given as

$$g_{back} = \bar{g} + G \cdot \frac{(M_e - \frac{4}{3}\pi\bar{\rho}(R_e^3 - r^3))}{r^2} \quad (9)$$

where  $G$  is the gravitational constant,  $R_e = 6371\text{km}$  and  $M_e = 5.972 \cdot 10^{24}\text{kg}$  are Earth’s mean radius and total mass, respectively.  $\bar{g} = 173.7\text{mGal}$  is the mean gravity removed from the data prior to inversion, replaced under the assumption that its source was sufficiently infinite and/or remote to provide only a constant throughout the domain. Consistent with the assumption of a spherical Earth for  $g_{back}$  the geocentric radius  $r$  is approximated as  $r \approx R_e + f_h \cdot h$  where  $h$  is the (negative) geodetic height and  $f_h$  is the height scaling factor, see equation (A.1). We account for the load of the oceans by applying a pressure boundary condition at zero geoid  $h = 0$  of

$$p_0 = \rho_{ocean} g_0 H_{ocean} \quad (10)$$

where  $\rho_{ocean} = 1030 \frac{\text{kg}}{\text{m}^3}$ ,  $g_0$  is  $9.81 \frac{\text{m}}{\text{s}^2}$  and  $H_{ocean}$  is the water column thickness in meters. This gives the total pressure (given by equation (7)), defined throughout the domain.

A central concept of classical isostasy is to define the isostatic compensation elevation, or elevations, the ideal case of which is defined by an elevation for which pressure is equal in all columns. To correctly visualise and analyse the isostatic state of our model, which has no topography, we must redefine our vertical dimension in terms of elevation relative to the geoid, rather than depth below the top of the crust.

In the 3D pressure field, shorter wavelength topography-derived pressure anomalies are attenuated with depth, and so it is necessary to also attenuate the topography correction. Therefore, we define a “pseudo-elevation” field throughout the domain. This correction takes into account topography and the smoothing of pressure variations with depth. To do this we first calculate the pressure  $p_{topo}$  due to topography loading by solving equation (7) given

$$F_\alpha = \rho_{topo} \cdot g_0 \delta_{h\alpha}. \quad (11)$$

As before, we apply a pressure boundary condition at zero geoid  $h = 0$  of

$$p_0 = -\rho_{topo} g_0 H_{topo} \quad (12)$$

where  $\rho_{topo}$  is a chosen density (we use  $\rho_{topo} = 2670 \frac{\text{kg}}{\text{m}^3}$ ) and  $H_{topo}$  is the topographic elevation relative to the geoid. A negative pressure anomaly for positive topography reverses the “flattening” of the surface earlier applied for the 3D gravity modelling. We then define “pseudo-elevation”  $\eta$  based on the relation

$$\eta = -\frac{p_{topo}}{\rho_{topo} \cdot g_0}. \quad (13)$$

Thus, the pseudo-elevation field  $\eta$  defines elevation, but is smoothed with depth in a manner consistent with the pressure results. For example, pseudo-elevation isosurfaces represent surfaces of consistent elevation relative to the geoid, taking into account the smoothing of the pressure field with depth. Note that the values chosen for  $\rho_{topo}$  and  $g_0$  do not matter, so long as they are consistent in equations (12) and (13).

Finally, to assist visualisation, we subtract from the total pressure a “background” pressure, which varies linearly with  $\eta$ , giving the residual “anomalous” pressure. The background pressure is defined by  $p_{back} = -\bar{\rho} \bar{g}_{back} \eta$ , where  $\bar{g}_{back}$  is the mean of  $g_{back}$ , see equation (9).

## 6 RESULTS AND DISCUSSION

### 6.1 The density and pressure models

The three model results for Australia’s lithospheric density and pressure fields at the three resolutions are fundamentally very similar, but have slightly different qualities with respect to the depth and magnitude of density changes as a result of the depth-sensitivities imposed by the horizontal mesh-dimensions. We focus discussion on the very-high resolution result because it is the fullest description of the lithospheric density and pressure fields. We note that the coarser resolution models are entirely adequate for their scale and may be preferable for certain uses.

The dominant features of this model are a strongly layered lithosphere, and a distinct contrast at all depths between the continental and oceanic domains (Figure 9). The crust has significant heterogeneity. These heterogeneities include major sedimentary basins, large crustal uplifts in central Australia, and distinct mid to lower crustal domains (Figure 9). The mantle has less heterogeneous density, however, the model resolves systematic differences between the density of the oceanic and continental regions, and some anomalous mantle regions in each domain.

Overall, the magnitude of the density correction,  $|m|$ , is relatively small, with a 95th percentile of  $\approx 50 \frac{\text{kg}}{\text{m}^3}$  and a median of  $14 \frac{\text{kg}}{\text{m}^3}$  (Figure 8). Therefore, for all but the most extreme changes, the density correction occurs within the uncertainty range typical of velocity to density conversion (Brocher 2005). In addition, the error thresholds of the reference model are not insignificant (Kennett & Salmon 2012), and the majority of the density changes in the model probably lie within these bounds. Although much of the large-scale structure was present in the reference model, there are significant and systematic changes from that model. Changes from the reference model include very significant detail added in the upper crust (see Figures A??, A??). These model changes persist quite strongly down into the mantle, albeit with reducing detail and magnitude with depth.

The pressure models are characterised by a strong contrast between the oceanic and continental domains. Within the oceanic domain, lateral variations in pressure are correlated with bathymetry, and by extension, the age of the oceanic lithosphere, with higher pressure beneath the youngest regions (cf. Figure 11, and Müller et al. (2008)), especially at the South East Indian Ridge. Narrow oceanic segments generate strong pressure anomalies that are not compensated, but attenuate significantly at elevations below  $-50\text{km}$  (see Figure ??). Variations of pressure within the continental region are quite weak, but are closely correlated with topography and the subsurface density field.

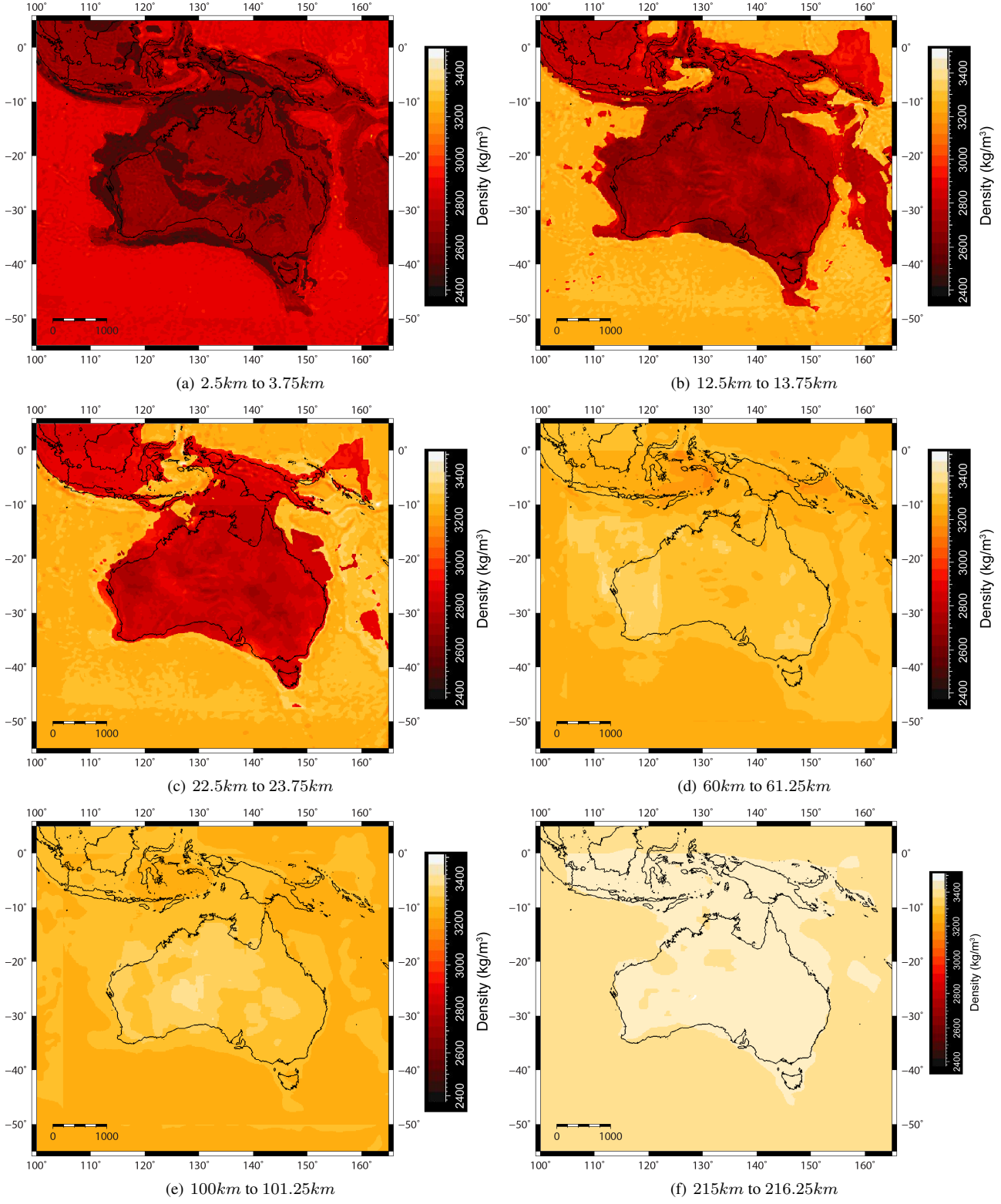


**Figure 9.** Slices through the very-high resolution density model at (a) 2.5km to 3.75km depth, (b) 12.5km to 13.75km depth, (c) 22.5km to 23.75km depth, (d) 60km to 61.25km depth, (e) 100km to 101.25km depth, and (f) 215km to 216.25km depth. Note that depths are depths below the top of the crust, not elevations.

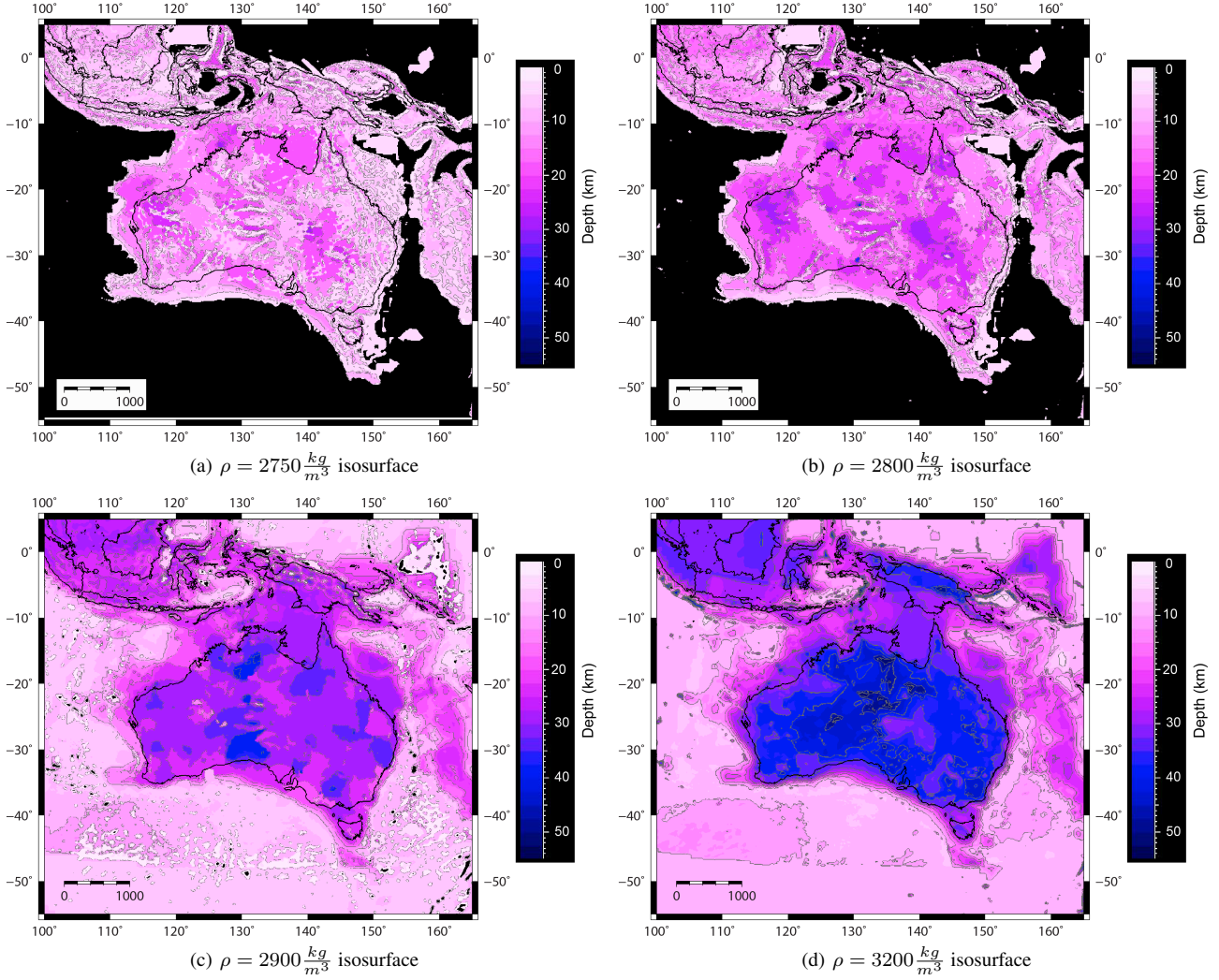


**Figure 10.** (a) The depth of the  $\rho = 2750 \frac{kg}{m^3}$  isosurface, taken as a proxy for the base of the felsic upper-crust; (b) the depth of the  $\rho = 2800 \frac{kg}{m^3}$  isosurface, taken as a proxy for the top of the mid-crust; (c) the depth of the  $\rho = 2900 \frac{kg}{m^3}$  isosurface, taken as a proxy for the top of the lower-crust and (d) the depth of the  $\rho = 3200 \frac{kg}{m^3}$  isosurface, taken as a proxy for the base of the crust. Note that depths are below the top of the crust, and therefore represent thicknesses.

## 6.2 Resolution and depth sensitivity

Repeated experiments at moderate and high resolutions have shown that the selection of inversion parameters  $\mu_1$  and  $\mu_0$  are not sensitive to the model resolution, and returned optimum values of  $\mu_1 = 0.005$  and  $\mu_0 = 10^{-7}$  for each resolution. Overall, the low variability of the acceptable models recovered from our parameter sweeps and consistency between resolutions indicates that the model result is robust across the tested model space. Variability analyses for each resolution showed that the overall density correction, and its variability with  $\mu$  followed a systematic form with depth for both  $\mu_1$  and  $\mu_0$  (Figures 6 and 8).

With  $\mu_1$  alone, the vertical density correction bias is defined by increasing  $|m|$  with depth (right panel in Figure 6). The choice of  $\mu_1$  will influence the level of  $H^1$ -regularization, that limits the gradients within  $m$ , and thus implicitly defines the length-scale of model changes. At this scale, gravity data have low sensitivity to vertical variations in  $m$ , but high sensitivity to lateral variations in  $m$ . Therefore, in the absence of  $L^2$ -regularization, the choice of

$\mu_1$ , and thus  $m$ , is defined primarily by the length-scale required to satisfy gravity variations across latitude,  $\phi$  and longitude,  $\lambda$ .

The mesh dimensions dictate a minimum Nyquist wavelength in  $\phi$  and  $\lambda$  of about 110km for the moderate resolution model, and about 55km for the high resolution model. Therefore, very small  $\mu_1$  values that would allow density corrections at wavelengths of less than this will not generate stable results, and are not likely to be accepted given the criteria used.

Further limits to the depth sensitivity of the model come from the natural increase of anomaly wavelength with source depth. Although the density correction in our model result is greatest in the lower half of the model, the variability across the accepted range of  $\mu_1$  is low for this depth range (Figure 6). At depth, the length-scale of  $m$  is not dictated by the limits imposed by  $\mu_1$ , but rather by the sensitivity of the gravity data, which do not require non-smooth density corrections at depth.

With both  $H^1$ - and  $L^2$ -regularization active, vertical density correction bias is towards reducing  $|m|$  with depth (Figure 8). The difference in  $|m|$  between the models with and without  $L^2$ -regularization is positive in the upper lithosphere and negative in

the lower lithosphere (right panel in Figure 8). For  $\mu_0$ , high variability is focused in the upper-lithosphere, although not the top few cells, and decays with depth.

The depth and resolution sensitivity to  $\mu_0$ , and the stable distance to origin (Figure 7) reflects the exchange of relatively expensive  $H^1$ -regularization for relatively inexpensive  $L^2$ -regularization. The inexpensiveness of  $L^2$ -regularization means that, even with small  $\mu_0$  values, large data misfits can be resolved with fairly minimal increases in the  $L^2$ -regularization term, but with significant reductions in the  $H^1$ -regularization term. Therefore, under increasing  $\mu_0$ , there is co-variance of the data-fit and regularization terms. For example, at moderate resolution, by increasing  $\mu_0$  from  $10^{-9}$  to  $10^{-7}$ , the data-fit term is reduced from  $5.88 \cdot 10^{-7}$  to  $3.85 \cdot 10^{-7}$  (65%); the  $L^2$  term increased from  $1.88 \cdot 10^{-7}$  to  $2.19 \cdot 10^{-7}$  (116%); but the  $H^1$ -regularization term is reduced from  $1.43 \cdot 10^{-7}$  to  $8.60 \cdot 10^{-9}$  (6%). The combined regularization term is reduced from  $3.32 \cdot 10^{-7}$  to  $2.28 \cdot 10^{-7}$  (69%). Similar results are obtained for the high-resolution model, although the improvement to gravity data misfit is greater.

Including  $L^2$ -regularization has permitted the inclusion of a crust with more heterogeneous density structure than with  $H^1$ -regularization alone. Figure 8 shows that, relative to the moderate resolution model, the high resolution model's density correction shows more intense peaks, but lesser average variability and a lower median density correction in the crust and uppermost mantle. This is because the  $L^2$ -regularization term allows the non-smooth gravity field to be satisfied with relatively low-cost density corrections at specific locations in the upper crust. The higher resolution model, and the higher resolution data, generate a greater degree of localisation, and thus the non-smooth gravity field is satisfied with less requirement for smooth density corrections extending to depth.

These tests show that the overall bias in the vertical distribution of the density correction is largely defined by the interaction between the chosen  $\mu_1$  and  $\mu_0$  and the model resolution in  $\phi$  and  $\lambda$ . In our final results, with both  $H^1$ - and  $L^2$ -regularization, the bias is towards a low amount of density correction in the uppermost 5km, the largest density correction in the upper and mid-crust, and reducing density correction towards the base of the model.

The presence of vertical bias is inherent to the gravity method in general and, although not always acknowledged, exists in all large-scale gravity models. Importantly, it does not mean that 3D structures are not resolved. However, it does mean that the depth extent of a feature can typically be considered a maximum depth, as constrained by the requirement to satisfy anomaly wavelengths, that "dipping" structures in the model result will typically be a maximum dip, as constrained by the requirement to match asymmetric gradients, and that complex multi-layer vertical structures will not spontaneously develop. Alternative methods exist to model such specific features more robustly (e.g. Aitken et al. 2013).

The reference model also carries significant uncertainty and artifacts. The most significant uncertainties for our results relate to those features that are unlikely to be rectified by our inversion. Recall that we apply regularization only to the density correction  $m$ , and not the total density field. Therefore, sharp features in the reference model are sustained unless they are highly incompatible with the gravity field. In general, this is desirable, as it allows for sharply defined features (such as sedimentary basins and the Moho) to be retained, but incorrect features may also be preserved. Taking into account the vertical bias of the method, the least likely to be rectified are errors in the vertical structure of the model (for example an erroneous crustal thickness). Non-smooth changes in the model, especially in the deeper parts of the model, are sustained also, for

example the sharp boundaries of the West Australian Craton lithospheric mantle are not substantially modified from the reference model.

### 6.3 3D tectonic architecture of the Australian Lithosphere

Australia's lithospheric density structure is well-layered, and interestingly, each layer possesses different structure, suggesting that different tectonic processes or events are preserved at different depths. The uppermost 5km is dominated by the presence of sedimentary basins, although some basement trends are represented also (Figure 9(a)). Deep sedimentary basins fringe the southern (Bight, Otway-Sorell, Bass and Gippsland basins), western (Perth Basin) and north-western (Carnarvon, Browse, Bonaparte and Ara-fura basins) margins of the continent, and are preserved in a WSW-ENE trending strip across the continental interior, including the Canning, Amadeus and Officer basins. The broad Eromanga Basin lies to the east of this, overlying the Thompson Orogen, and further east the Queensland, and Bowen and Sydney basins are aligned in a N-S belt. Thinner Cenozoic basins (e.g. Murray Basin, Eucla Basin) are not preserved in the model.

The crystalline upper-crust (Figures 9(b), 10(a)) is dominated by the well known tectonic regions (Figure 1(b)), and structure at these depths accords with the structure defined by previous "2D" gravity studies (Milligan et al. 2003; Shaw et al. 1996). Some prominent features include the Musgrave and Arunta provinces in central Australia, the Albany Fraser Province, the Kimberley Craton, the Mount Isa Province and North-East Queensland terranes, the subdivisions of the West Australian Craton and the Thompson, Lachlan and New England Orogens (see Figure 1(b) for locations). This suggests that the majority of the interpretable gravity field is sourced from the upper crust. Significant structure is also generated for this depth within Sundaland, New Guinea, and in the Lord-Howe Rise, regions that had little structure in the reference model. Several parts of New Guinea have high-density, even mafic density, rocks predicted for the near surface (Figures 10(b), 10(c)). These are in accordance with the locations of ophiolites, including the Irian Ophiolite Belt and the Papuan Ultramafic Belt, and a third region that corresponds with the Ertsberg mining district (Baldwin et al. 2012).

The mid-crust (Figures 9(c), 10(b)) possesses a more prominent WNW-ESE grain that parallels the intraplate sedimentary basins. The Canning, Amadeus and Eromanga Basins are underlain by lower-density crust (cf. Figures 9(a), 9(c)). This carries the implication that the formation and preservation of intraplate sedimentary basins may be related to the density structure of the mid-to-lower crust. These regions contain several lithospheric scale structures associated with the growth of the Australian continent, and it is likely that these have remained loci for intraplate deformation and basin formation. The northern margin of the undeformed Australian continent in New Guinea is well imaged, with low density crust to the south and higher density crust within the orogen to the north (Figure 9(c)).

The lower crust and Moho possess different structure again. Crustal thickness (Figure 10(d)) bears little resemblance to topography and the upper crust, and bears only some resemblance to the mid-crust. The thickness of the non-mafic crust, with density less than  $2900 \frac{kg}{m^3}$  is relatively constant, except in certain areas (Figure 10(c)). This suggests that the topography of the Moho (Figure 10(d)) largely depends on the thickness of the high-density lower crust. Three distinct regions can be identified: southwestern central Australia, northern Australia and the eastern Thompson Oro-

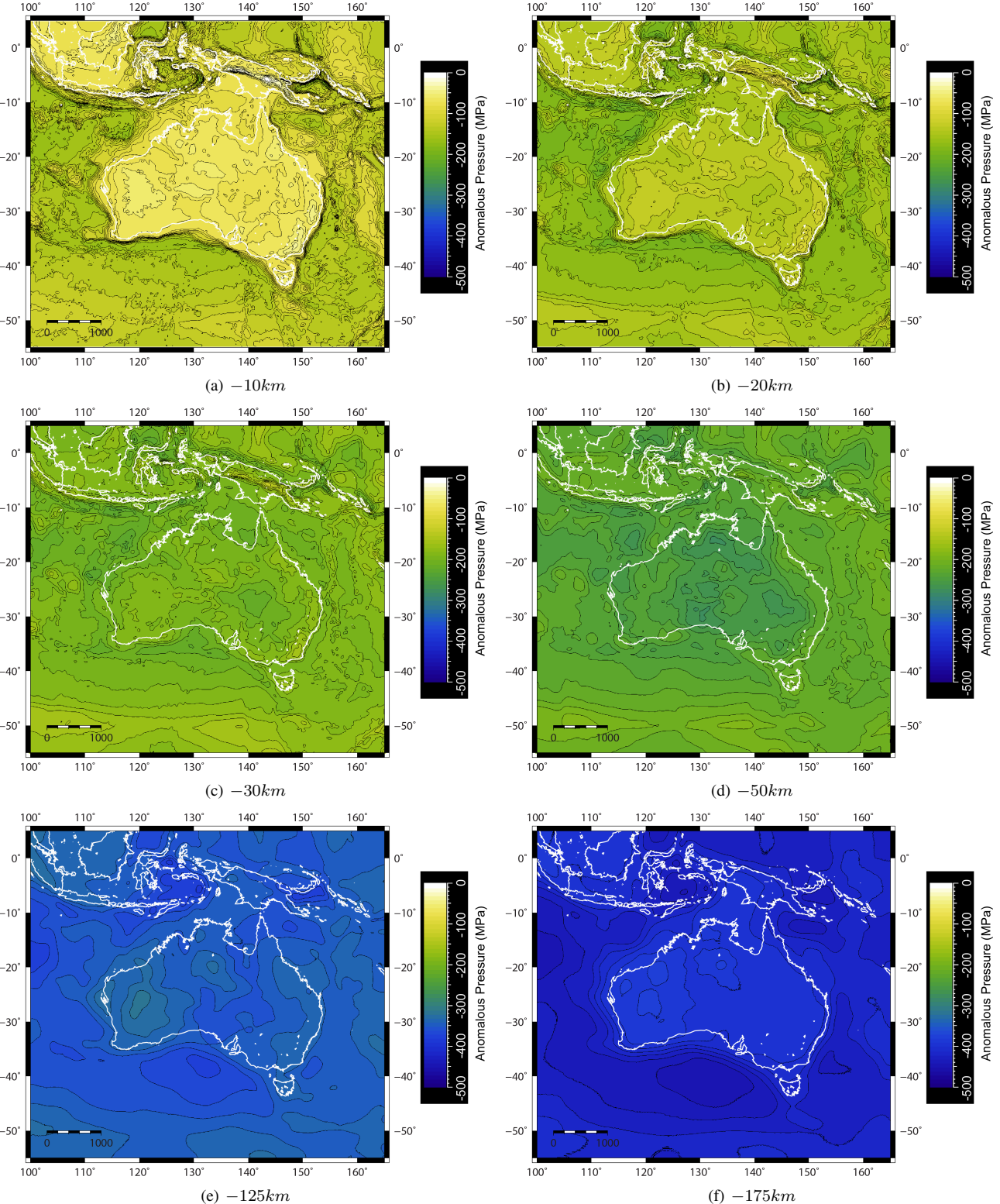


**Figure 11.** Slices through the anomalous pressure model at pseudo-elevations of  $-10\text{ km}$  (a),  $-20\text{ km}$  (b),  $-30\text{ km}$  (c),  $-50\text{ km}$  (d),  $-125\text{ km}$  (e) and  $-175\text{ km}$  (f).

gen. This thick, dense and probably mafic lower crust is imaged in several deep seismic reflection and refraction experiments, as well as receiver functions for the relevant areas (Clitheroe et al. 2000; Drummond & Collins 1986; Finlayson et al. 1980). The recent Yilgarn-Officer-Musgrave line in western-central Australia identified an extensive low-reflectivity lower-crustal province approximately 15 km thick (Howard et al. 2013). Previous studies have attributed very thick crust in these regions to magmatic underplating (Aitken 2010; Drummond & Collins 1986; Finlayson et al. 1980). Thinner crust in parts of eastern and western Australia has a much greater proportion of felsic to intermediate crust, with little mafic crust, e.g. the Pilbara Craton and western Thompson Orogen possess almost entirely low-density crust (cf Figure 10(c), 10(d)).

Within the lithospheric mantle, the principal subdivision is between the continental and oceanic domains, and within the continent, between the Archean West Australian Craton, mostly higher density, the Archean to Proterozoic central portion, mostly moderate to high density, and the mostly Phanerozoic eastern portion, which is moderate density (Figure 9(d), 9(e)). The boundaries between these domains are oriented close to north-south, and are located at approximately 120°E to 125°E and 140°E to 145°E.

Prior studies of the Precambrian to Phanerozoic transition have indicated a series of steps in lithospheric thickness from west to east, stepping up from  $> 200\text{km}$  thick beneath the craton to  $\approx 50\text{km}$  beneath the Southeastern Highlands (Fishwick et al. 2008). The thinner lithosphere in the east is consistent with our observation of lower density of Phanerozoic lithospheric mantle in the final model due to higher temperatures (Figure 9(e)). We note that, although the final density is less, the density correction is strongly positive for the region east of  $\approx 142^\circ\text{E}$ , increasing at lithospheric mantle depths from  $0 - 10 \frac{\text{kg}}{\text{m}^3}$  under the craton to  $50 \frac{\text{kg}}{\text{m}^3}$  under the Eastern Highlands (Figure A??).

Numerous studies have shown that Precambrian and especially Archean mantle lithosphere is typically more depleted than Phanerozoic mantle lithosphere, and that more-depleted mantle is less dense than less-depleted mantle (see for example Kaban et al. 2014; Tesauro et al. 2014; Poudjom Djomani et al. 2001). Except for part of the West Australian Craton, the original density conversion from velocity did not account for this difference in composition (Kennett et al. 2013) and so our density correction rectifies the resulting mass deficit/surplus. The geometry and magnitude of the positive density correction over eastern Australia is compatible with the interpretation of Fishwick et al. (2008) who propose a transition from Archean to Early-Proterozoic lithosphere west of  $\approx 140^\circ\text{E}$  to Phanerozoic lithosphere fringing the continental margin.

Superimposed upon this are several shorter-wavelength features. These include high-density regions at  $\approx -100\text{km}$  depth beneath the regions with thicker crust (Figure 9(e)). Low density regions within Western Australia are features of the reference model density conversion function (Kennett et al. 2013). Below approximately 150 km, the density structure becomes quite homogeneous, but with a clear difference still between higher-density continental regions and the lower-density oceanic regions, as well as the major lithospheric regions noted previously (Figure 9(f)). The more homogeneous density structure at depth is primarily a result of the reduction in the sensitivity of gravity data to shorter wavelength structure at depth, rather than necessarily representing the real structure of the lithosphere.

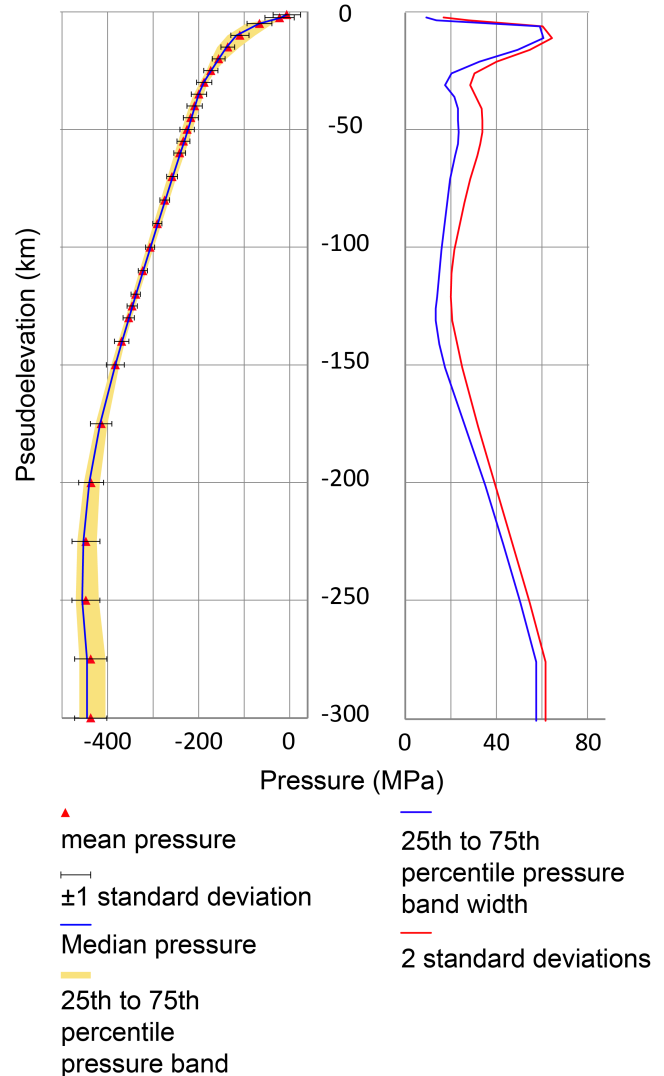


**Figure 12.** Pressure variability with depth, showing pressure anomaly and its variation sampled on pseudoelevation isosurfaces. Left: median and mean anomalous pressure including variability measures. Right: Pressure variability expressed as two standard deviations and the width of the 25th to 75th percentile band. Except the uppermost crust, the minimum variability within the model is reached at  $-120$  to  $-130\text{ km}$ , with a subsidiary minimum at  $\approx -30\text{ km}$ . Peaks are observed at  $-10\text{ km}$  and at  $-45$  to  $-50\text{ km}$ , with the highest values observed at the base of the model.

#### 6.4 Isostatic Equilibration of the Australian Continent

Density and gravity variations contained in our model, as well as the water load from the oceans, generate significant pressure variations. Within the upper continental crust, pressure anomalies reduce in magnitude downwards until approximately  $-30\text{km}$  elevation (cf. Figures 11(a), 11(b); 11(c)). By  $-30\text{km}$  elevation (Figure 11(b)) the majority of intracontinental pressure variations are absent, with the exception of fairly narrow highs beneath the New Guinea highlands, the southeastern highlands of the mainland and Tasmania, a large low in the Eromanga Basin region and smaller magnitude broad highs in central and western Australia. This pressure model suggests that a significant amount of isostatic compensation is achieved by  $-30$  to  $-35\text{ km}$  elevation (Figure 12). This depth range is similar to the base of the non-mafic crust, defined by the  $2900 \frac{\text{kg}}{\text{m}^3}$  density isosurface (Figure 10(c)). This suggests that

much of the density contrast between the Australian continent and the Indian Ocean and Tasman Seas, and a large proportion of topography and upper crustal loads within the continent, are compensated by variations in the thickness of the felsic-intermediate crust.

Pressure within the uppermost continental mantle (Figures 11(d)) strongly reflects crustal thickness, and some crustal density heterogeneities (e.g. the low-density Pilbara Craton, the Musgrave and Arunta Provinces), and mantle density heterogeneities (e.g. the West Australian Craton). Pressure variability at  $-50\text{km}$  is greater than at  $-30\text{km}$  (cf. Figures 11(c) 11(d)). Most notable is the large pressure low developed beneath central-eastern Australia, beneath the regions of thick crust (Figure 10(d)). This implies that the overthickened lower crust of Australia, below  $-35\text{km}$  elevation, is a source of isostatic disequilibrium.

This anomalously low pressure in central Australia's lithospheric mantle is eventually compensated by high-density mantle by around  $-100\text{km}$  elevation (Figure 9(e)), and by  $-125\text{km}$  pressure is close to background values (Figure 11(e)). This elevation range show the lowest variability of all elevations within the model (Figure 12). However, in western Australia, where the crust is thinner, and the deep-mantle is of mostly high density, relatively high pressure extends from  $-75\text{km}$  to an elevation of  $-200\text{km}$ .

Small loads, such as those in central Australia, may be sustained by the rigidity of the lithosphere. Pressure anomalies from uncompensated loads persist well into the mantle, but reduce in intensity with depth as they are attenuated, reaching negligible values at approximately  $-100\text{km}$  to  $-150\text{km}$  elevation depending on width. The New Guinea Highlands possess thick crust, but are only partly compensated, with excess pressure persisting to  $-100\text{km}$  elevation. High topography in eastern and southeastern Australia generates high pressure down to an elevation of approximately  $-150\text{km}$ . This region is only partially compensated by thick crust and mantle density, and the excess pressure from topography is reduced through pressure attenuation. This region has previously been inferred to possess significant dynamic support of topography (Czarnota et al. 2014).

Within the oceanic region, the Indian Ocean and the South Australian Basin possess the deepest bathymetry, and therefore the lowest pressures in the upper lithosphere. Within the Indian Ocean, pressure beneath the Wharton Basin and Argo Abyssal Plain is less than beneath the Perth Abyssal Plain. The oceanic lithosphere may be somewhat denser to the north below  $50\text{km}$  depth (Figures 9(d), 9(e)), and by  $-100\text{km}$  elevation the pressure discrepancy is minimal. The Tasman Sea does not show a clear relationship with age, instead showing fairly consistent pressures throughout. Within the Southern Ocean, pressure is highest at the Southeast Indian Ridge and reduces northwards, largely in line with increasing oceanic lithosphere age and deeper bathymetry. Southern Ocean bathymetry is not compensated in this model, perhaps representing dynamic support of topography. Neither dynamic support from the mantle, nor the gravity effects of mantle temperature (Chappell & Kusznir 2008), are included in our model and so the younger Southern Ocean is not well described by this model.

The pressure effects of narrow oceanic segments, such as the northern Tasman Sea, Coral Sea, Celebes Sea, Banda Sea and Solomon Sea, are controlled by pressure-attenuation, rather than oceanic age. The Pacific Ocean lies outside the AuSREM region, but the pressure differences in this region are largely equilibrated by  $-30\text{ km}$  elevation, although the Ontong-Java Plateau may possess overthickened crust, and the pressure effects of the ridge in the Caroline Sea are also sustained to depth.

Below  $-125\text{km}$  elevation, the pressure model is characterised by relatively high-pressure beneath the continental region, and relatively low-pressure beneath the oceanic regions. This pressure is driven by the mantle density, which is higher in the continental regions than in the oceanic regions (see Figure 9(f)). This is a feature of the reference model, derived from the S-wavespeed model (see Kennett et al. (2013) for the derivation of density), although our model has tended to reinforce the difference (Figure ??). The uncertainties in both the reference model and the gravity inversion results mean that these depths cannot be easily interpreted with confidence. However, if valid, the results imply a need for a compensatory buoyancy force in the upper mantle, involving low-density upper mantle beneath the continent and high-density upper mantle beneath the oceans.

## 7 CONCLUSION

Using a new gravity inversion method, capable of reliably modelling the gravity effects of deep lithospheric density structure, Australia's lithospheric density field and its corresponding pressure field have been characterised. This model is built upon, and is consistent with, the *AuSREM* seismological model (Kennett et al. 2013; Salmon et al. 2013a; Kennett & Salmon 2012) and satisfies the gravity field for wavelengths between  $\frac{1}{4}^\circ$  and  $12^\circ$ . Thorough parameter sweeps for the main inversion parameters indicate that model variability within the acceptable range is low. Valid results were generated for three model resolutions,  $\frac{1}{2}^\circ$ ,  $\frac{1}{4}^\circ$  and  $\frac{1}{8}^\circ$  all similar, but with slightly differing responses at depth. The results contain many significant tectonic features that were not present in the prior model, and allow the 3D tectonic architecture of the continent, and its isostatic compensation depths, to be analysed in detail. We show that both the density and pressure models are inherently layered, that there is significant structural complexity in the mid-crust to lithospheric-mantle, and that this differs from structure in the uppermost crust. Complete isostatic compensation is never achieved, but pressure differences are relatively low at elevations of  $-30\text{km}$ , and lowest between  $-125\text{km}$  and  $-150\text{km}$  elevation (Figure 12). We interpret this to suggest that the base of the felsic-intermediate crust and the base of mature oceanic lithosphere are the main compensation surfaces for the Australian continent.

## 8 ACKNOWLEDGEMENTS

This research was supported by a UWA/UQ Bilateral Research Collaboration Award. This work was supported by resources provided by the Pawsey Supercomputing Centre with funding from the Australian Commonwealth Government and the Government of Western Australia, including their support through the Petascale Pioneers Program. The development of *escript* was undertaken as part of the AGOS EIF and AuScope NCRIS funded by the Australian Commonwealth Government. Gravity data was provided by the ICGEM, Potsdam, Germany. Peter Kovacs provided perceptually uniform colour scales (available at <http://peterkovacs.com/projects/colourmaps/>). The *AuSREM* model components were developed through AuScope, and were provided by the Australian National University. The authors wish to thank Jörg Ebbing and an anonymous reviewer for their comments and the editor for handling the manuscript promptly. *escript* is available from <https://launchpad.net/escript>.

finley and the results of this project are available from <https://github.com/al8ken/FEILDSAustralia.git>.

## REFERENCES

- Afonso, J., Fullea, J., Griffin, W., Yang, Y., Jones, A., Yang, Y., Connolly, J., & Reilly, S., 2013a. 3-d multiobservable probabilistic inversion for the compositional and thermal structure of the lithosphere and upper mantle. i: A priori petrological information and geophysical observables, *Journal of Geophysical Research: Solid Earth*, **118**(5), 2586–2617.
- Afonso, J., Fullea, J., Yang, Y., Connolly, J., & Jones, A., 2013b. 3-d multi-observable probabilistic inversion for the compositional and thermal structure of the lithosphere and upper mantle. ii: General methodology and resolution analysis, *Journal of Geophysical Research: Solid Earth*, **118**(4), 1650–1676.
- Aitken, A., 2010. Moho geometry gravity inversion experiment (MoGGIE): A refined model of the Australian Moho, and its tectonic and isostatic implications, *Earth and Planetary Science Letters*, **297**(1-2), 71–83.
- Aitken, A., Salmon, M., & Kennett, B., 2013. Australia's Moho: A test of the usefulness of gravity modelling for the determination of Moho depth, *Tectonophysics*, **609**, 468–479.
- Amante, C. & Eakins, B., 2009. ETOPO1 1 Arc-Minute Global Relief Model: Procedures, Data Sources and Analysis, *ETOPO1 1 Arc-Minute Global Relief Model: Procedures, Data Sources and Analysis*, p. 19.
- Baldwin, S. L., Fitzgerald, P. G., & Webb, L. E., 2012. Tectonics of the New Guinea Region, *Annual Review of Earth and Planetary Sciences*, **40**(1), 495–520.
- Brocher, T., 2005. Empirical relations between elastic wavespeeds and density in the Earth's crust, *Bulletin of the Seismological Society of America*, **95**(6), 2081–2092.
- Carlson, R. & Raskin, G., 1984. Density of the ocean crust, *Nature*, **311**(5986), 555–558.
- Chappell, A. & Kusznir, N., 2008. Three-dimensional gravity inversion for Moho depth at rifted continental margins incorporating a lithosphere thermal gravity anomaly correction, *Geophysical Journal International*, **174**(1), 1–13.
- Clitheroe, G., Gudmundsson, O., & Kennett, B., 2000. The crustal thickness of australia, *Journal of Geophysical Research: Solid Earth*, **105**(B6), 13697–13713.
- Czarnota, K., Roberts, G. G., White, N. J., & Fishwick, S., 2014. Spatial and temporal patterns of Australian dynamic topography from River Profile Modeling, *Journal of Geophysical Research: Solid Earth*, **119**(2), 1384–1424.
- Drummond, B. & Collins, C., 1986. Seismic evidence for underplating of the lower continental crust of australia, *Earth and Planetary Science Letters*, **79**(3-4), 361–372.
- Featherstone, W. & Claessens, S., 2008. Closed-Form transformation between geodetic and ellipsoidal coordinates, *Studia Geophysica et Geodaetica*, **52**(1), 1–18.
- Finlayson, D., Collins, C., & Denham, D., 1980. Crustal structure under the lachlan fold belt, southeastern australia, *Physics of the Earth and Planetary Interiors*, **21**(4), 321–342.
- Fishwick, S., Heintz, M., Kennett, B., Reading, A., & Yoshizawa, K., 2008. Steps in lithospheric thickness within eastern australia, evidence from surface wave tomography, *Tectonics*, **27**(4).
- Förste, C., Bruinsma, S., Flechtner, F., Abrikosov, O., Dahle, C., Marty, J., Lemoine, J., Biancale, R., Barthelmes, F., Neumayer, K., & König, R., 2013. EIGEN-6C3 - The latest Combined Global Gravity Field Model including GOCE data up to degree and order 1949 of GFZ Potsdam and GRGS Toulouse, *AGU Fall Meeting Abstracts*, p. A860.
- Foulger, G., Panza, G., Artemieva, I., Bastow, I., Cammarano, F., Evans, J., Hamilton, W., Julian, B., Lustriño, M., Thybo, H., & Yanovskaya, T., 2013. Caveats on tomographic images, *Terra Nova*, **25**(4), 259–281.
- Frogtech, 2005. OZ SEEBASE Study 2005, Public Domain Report to Shell Development Australia by FrOG Tech Pty Ltd.
- Fullea, J., Afonso, J., Connolly, J., Fernández, M., García-Castellanos, D., & Zeyen, H., 2009. Litmod3d: An interactive 3-d software to model the thermal, compositional, density, seismological, and rheological structure of the lithosphere and sublithospheric upper mantle, *Geochemistry, Geophysics, Geosystems*, **10**(8).
- Gross, L. & Kemp, C., 2013. Large Scale Joint Inversion of Geophysical Data using the Finite Element Method , in *ASEG Extended Abstracts*, pp. 1–4.
- Gross, L., Bourguin, L., Hale, A. J., & Muhlhaus, H. B., 2007. Interface Modeling in Incompressible Media using Level Sets in Escript, *Physics of the Earth and Planetary Interiors*, **163**, 23–34.
- Gross, L., Altinay, C., & Shaw, S., 2015. Inversion of potential field data using the finite element method on parallel computers, *Computers & Geosciences*, **84**, 61 – 71.
- Howard, H., Quentin de Gromard, R., Smithies, R., Kirkland, C., Wingate, M., Aitken, A., Korsch, R., Gessner, K., Blewett, R., Pawley, M.J. and Gorczyk, W., Carr, L., Neumann, N., Holzschuh, J., Duan, J., Goodwin, J., & Jones, T., 2013. Geological setting and interpretation of the northeastern half of deep seismic reflection line 11gay01: west musgrave province and the bentley supergroup, *Geoscience Australia Record*, **28**, 51–95.
- Kaban, M., Tesauro, M., Mooney, W., & Cloetingh, S., 2014. Density, temperature, and composition of the north american lithosphere - new insights from a joint analysis of seismic, gravity, and mineral physics data: 1. density structure of the crust and upper mantle, *Geochemistry, Geophysics, Geosystems*, **15**(12), 4781–4807.
- Kennett, B. & Salmon, M., 2012. AuSREM: Australian Seismological Reference Model, *Australian Journal of Earth Sciences*, **59**(8), 1091–1103.
- Kennett, B., Fichtner, A., Fishwick, S., & Yoshizawa, K., 2013. Australian seismological reference model (AuSREM): Mantle component, *Geophysical Journal International*, **192**(2), 871–887.
- Lafehr, T., 1991. An exact solution for the gravity curvature (Bullard B) correction, *Geophysics*, **56**(8), 1179–1184.
- Laske, G., Masters, G., Ma, Z., & Pasyanos, M., 2012. CRUST1.0: An Updated Global Model of Earth's Crust, in *EGU General Assembly Conference Abstracts*, vol. 14 of *EGU General Assembly Conference Abstracts*, p. 3743.
- Li, Y. & Oldenburg, D., 1998. 3D inversion of gravity data, *Geophysics*, **63**, 109–119.
- Milligan, P., Petkovic, P., & Drummond, B., 2003. Potential-field datasets for the Australian region: Their significance in mapping basement architecture, *Special Paper of the Geological Society of America*, **372**, 129–139.
- Müller, R., Sdrolias, M., Gaina, C., & Roest, W., 2008. Age, spreading rates, and spreading asymmetry of the world's ocean crust, *Geochemistry, Geophysics, Geosystems*, **9**(4).
- Nowell, D., 1999. Gravity terrain corrections - an overview, *Journal of Applied Geophysics*, **42**(2), 117–134.
- Pail, R., Bruinsma, S., Migliaccio, F., Förste, C., Goiginger, H., Schuh, W.-D., Höck, E., Reguzzoni, M., Brockmann, J., Abrikosov, O., Veichert, M., Fecher, T., Mayrhofer, R., Krasbutter, I., Sansò, F., & Tscherning, C., 2011. First GOCE gravity field models derived by three different approaches, *Journal of Geodesy*, **85**(11), 819–843.
- Pavlis, N., Holmes, S., Kenyon, S., & Factor, J., 2012. The development and evaluation of the Earth Gravitational Model 2008 (EGM2008), *Journal of Geophysical Research: Solid Earth*, **117**(4).
- Poudjom Djomani, Y., O'Reilly, S., Griffin, W., & Morgan, P., 2001. The density structure of subcontinental lithosphere through time, *Earth and Planetary Science Letters*, **184**(3-4), 605–621.
- Salmon, M., Kennett, B., & Saygin, E., 2013a. Australian seismological reference model (AuSREM): Crustal component, *Geophysical Journal International*, **192**(1), 190–206.
- Salmon, M., Kennett, B., Stern, T., & Aitken, A., 2013b. The Moho in Australia and New Zealand, *Tectonophysics*, **609**, 288–298.
- Seton, M., Müller, R., Zahirovic, S., Gaina, C., Torsvik, T., Shephard, G., Talsma, A., Gurnis, M., Turner, M., Maus, S., & Chandler, M., 2012. Global continental and ocean basin reconstructions since 200Ma, *Earth-Science Reviews*, **113**(3-4), 212–270.

- Shaw, R., Wellman, P., Gunn, P., Whitaker, A., Tarlowski, C., & Morse, M., 1996. Guide to using the Australian crustal elements map. *Australian Geological Survey Organisation Record*, **30**.
- Simmons, N., Forte, A., Boschi, L., & Grand, S., 2010. Gypsum: A joint tomographic model of mantle density and seismic wave speeds. *Journal of Geophysical Research: Solid Earth*, **115**(12).
- Tapley, B., Bettadpur, S., Watkins, M., & Reigber, C., 2004. The gravity recovery and climate experiment: Mission overview and early results. *Geophysical Research Letters*, **31**(9), L09607 1–4.
- Tesuaro, M., Kaban, M., Mooney, W., & Cloetingh, S., 2014. Density, temperature, and composition of the north american lithosphere - new insights from a joint analysis of seismic, gravity, and mineral physics data: 2. thermal and compositional model of the upper mantle. *Geochemistry, Geophysics, Geosystems*, **15**(12), 4808–4830.
- Wessel, P., Smith, W. H. F., Scharroo, R., Luis, J., & Wobbe, F., 2013. Generic mapping tools: Improved version released. *Eos, Transactions American Geophysical Union*, **94**(45), 409–410.
- Zienkiewicz, O. C., Taylor, R. L., & Zhu, J. Z., 2013. *The Finite Element Method: Its Basis and Fundamentals*, Elsevier, Oxford, 7th edn.

## APPENDIX A: GEODETIC COORDINATE SYSTEM

We use the Geodetic Coordinate system in  $(\phi, \lambda, h)$  where a location of a point  $(x, y, z)$  is described by its geodetic latitude  $\phi$  (in deg), longitude  $\lambda$  (in deg) and geodetic height  $h$  (in km), see Featherstone & Claessens (2008). The coordinates  $(x, y, z)$  are given in the form

$$\begin{aligned} x &= (N + f_h \cdot h) && \cdot \cos(f_a \cdot \phi) \cdot \cos(f_a \cdot \lambda) \\ y &= (N + f_h \cdot h) && \cdot \cos(f_a \cdot \phi) \cdot \sin(f_a \cdot \lambda) \\ z &= (N \cdot (1 - e^2) + f_h \cdot h) && \cdot \sin(f_a \cdot \phi) \end{aligned} \quad (\text{A.1})$$

where the geodetic zero level  $N$  is given as

$$N = \frac{R_e}{\sqrt{1 - e^2 \cdot \sin^2(f_a \cdot \phi)}} \quad (\text{A.2})$$

with the semi-major axis length  $R_e$  of the Earth and its eccentricity  $e$ . The factors  $f_a$  and  $f_h$  consider the change of units from deg to rad and km to m, respectively. For the WGS84 reference system used in this paper we have  $R_e = 6378.1370\text{km}$  and eccentricity  $e = 0.08181919084262149$ . The reference model is defined in a geocentric coordinate system but is not corrected for the geodetic coordinate system as the reference model is providing an initial density distribution for the inversion only.

As the geodetic coordinate system chosen here is orthogonal the gravitation along the coordinate lines  $\alpha = \phi, \lambda, h$  are given in the form

$$g_\alpha = -d_\alpha \frac{\partial u}{\partial \alpha} \quad (\text{A.3})$$

with the scaling factors

$$\begin{aligned} d_\lambda &= \frac{1}{f_a \cdot (N + f_h \cdot h) \cdot \cos(f_a \cdot \phi)}, \\ d_\phi &= \frac{1}{f_a \cdot (M + f_h \cdot h)} \text{ and} \\ d_h &= \frac{1}{f_h} \end{aligned}$$

where

$$M = \frac{R_e \cdot (1 - e^2)}{(1 - e^2 \cdot \sin^2(f_a \cdot \phi))^{\frac{3}{2}}} \quad (\text{A.4})$$

Moreover for integrals we get by substitution rule

$$dx \, dy \, dz = V \, d\phi \, d\lambda \, dh \quad (\text{A.5})$$

with

$$V = (d_\phi d_\lambda d_h)^{-1}. \quad (\text{A.6})$$

The differential equations (6) for gravity potential and (7) for pressure are solved in variational form using the finite element method (Zienkiewicz et al. 2013). Using the geodetic coordinate system the variational form for the solution  $u$  is given as

$$\int_{\Omega} \left( d_\lambda^2 \frac{\partial v}{\partial \lambda} \frac{\partial u}{\partial \lambda} + d_\phi^2 \frac{\partial v}{\partial \phi} \frac{\partial u}{\partial \phi} + d_h^2 \frac{\partial v}{\partial h} \frac{\partial u}{\partial h} \right) V \, d\phi \, d\lambda \, dh = Q(v) \quad (\text{A.7})$$

for all sufficiently smooth functions  $v$ . For the gravity potential

$$Q(v) = 4\pi G \cdot \int_{\Omega} \rho v \, d\phi \, d\lambda \, dh \quad (\text{A.8})$$

and for the static pressure

$$Q(v) = \int_{\Omega} \left( d_\lambda \frac{\partial v}{\partial \lambda} F_\lambda + d_\phi \frac{\partial v}{\partial \phi} F_\phi + d_h \frac{\partial v}{\partial h} F_h \right) V \, d\phi \, d\lambda \, dh \quad (\text{A.9})$$

where  $F$  is the internal force density as defined in equation (8).

## APPENDIX B: PRESSURE EQUATION DERIVATION

We derive equation (7) for the pressure field  $p$ . The stress state  $\sigma$  due to a body force  $\mathbf{F}$  fulfills the conservation of momentum equations

$$-\nabla^t \sigma = \mathbf{F}. \quad (\text{B.1})$$

The stress tensor can be written in the form

$$\sigma = \sigma' - p I \quad (\text{B.2})$$

where  $\sigma'$  denotes the deviatoric stress and  $I$  is the identity tensor. This is inserted into equation (B.1) and the divergence operator  $\nabla^t$  is applied to obtain

$$-\nabla^t(\nabla^t \sigma') + \Delta p = \nabla^t \mathbf{F}. \quad (\text{B.3})$$

Under the assumption of an isotropic elastic Earth the deviatoric stress is proportional to the deviatoric strain  $\varepsilon'$  in the form

$$\sigma' = 2G_s \varepsilon' \quad (\text{B.4})$$

with shear modulus  $G_s$ . In Cartesian coordinates  $(x_i)$  the deviatoric strain is given as

$$\varepsilon'_{ij} = \frac{1}{2} \left( \frac{\partial u_i}{\partial x_j} + \frac{\partial u_j}{\partial x_i} \right) - \frac{1}{3} \delta_{ij} \sum_k \frac{\partial u_k}{\partial x_k} \quad (\text{B.5})$$

with the the displacement  $\mathbf{u} = (u_i)$  resulting from the external force  $\mathbf{F}$ . With this we see that in fact identity

$$-\nabla^t(\nabla^t \varepsilon') = \sum_{ij} \frac{\partial^2 \varepsilon'_{ij}}{\partial x_i \partial x_j} = 0 \quad (\text{B.6})$$

holds. Under the additional assumption that the shear modulus  $G_s$  is constant we can also immediately conclude that  $\nabla^t(\nabla^t \sigma') = 0$ . This establishes equation (7) from equation (B.3).

The partial differential equation (7) is solved for pressure  $p$  below the geodetic zero surface using the geodetic coordinate system, see Appendix A. On other faces except the zero geoid  $h = 0$  we use the boundary conditions

$$\mathbf{n}^t \nabla p = \mathbf{n}^t \mathbf{F} \quad (\text{B.7})$$

where  $\mathbf{n}$  defines the outer normal field on the surface of the computational domain. Combining equation (B.1) and equation (B.2) shows that this boundary condition implies a constant deviatoric stress near and perpendicular to the boundary.